Numerical Investigation of Tsunami Bore Effects on Structures, Part I: Drag Coefficients

Nora Asadollahi

Formerly MSc student, Department of Civil Engineering, University of Ottawa, 161 Louis Pasteur, Ottawa, ON, Canada, K1N 6N5. E-mail: nasad010@uottawa.ca

Ioan Nistor

Professor, Department of Civil Engineering, University of Ottawa, 161 Louis Pasteur, Ottawa, ON, Canada, K1N 6N5. E-mail: inistor@uottawa.ca

Abdolmajid Mohammadian

Professor, Department of Civil Engineering, University of Ottawa, 161 Louis Pasteur, Ottawa, ON, Canada, K1N 6N5. E-mail: amohamma@uottawa.ca

Abstract

Recent tsunami disasters caused devastating damage to non-engineered as well as engineered coastal infrastructure. In fact, previous design guidelines containing provisions for tsunami loading did not provide accurate estimations of tsunami loads in order to design structures capable of withstanding tsunami impacts. The drag coefficient plays a significant role in the calculation of tsunami hydrodynamic forces. This coefficient is traditionally calculated based on a steady flow analogy. However, tsunami-induced coastal inundation is a typical case of rapidly-varying unsteady flows. The present study aims at investigating the tsunami forces exerted on structures with different geometries in order to provide realistic guidelines to estimate drag coefficients for unsteady flows. In this paper, a dam-break wave is used to investigate the tsunami-induced bore interaction with structures. A three-dimensional multiphase numerical model is implemented to study the tsunami loading on rectangular-shaped structures with various aspect ratios (width/depth) and orientations. The numerical model results are validated using measured forces and bore surface elevations from physical experiments previously carried out by some of the authors of this paper. A scaled-up domain is then modeled in order to

assess the performance of the model and the induced tsunami loading at prototype scale. The drag coefficient relations for various structural geometries and bore depths are further provided. The calculated hydrodynamic forces and associated drag coefficients are compared with data in the existing literature and current design codes.

Keywords: Hydrodynamic force, Drag coefficient, Rectangular column, Aspect ratio, Structure orientation

1. Introduction

Tsunamis are rare but devastating occurrences mainly caused by a submarine ocean bottom disturbance generated by an earthquake. Other generating factors such as landslides, volcanic eruptions and meteorite strikes can also produce devastating tsunami waves. The 2004 Indian Ocean Tsunami and the 2011 Great Japan Tohoku Tsunami inflicted extensive devastation along long stretches of coastal regions (Saatcioglu et al., 2005, Ghobarah et al. 2006, Yeh et al., 2007; Yeh et al., 2013). Following the 2011 Great Japan Tsunami, Mori et al. (2012), conducted a survey of inundation and run-up height along the north-eastern coast of Japan and reported average 10-15m run-up height and some localized values larger than 30m run-up in some areas. According to Yeh et al. (2013), reinforced concrete buildings failed substantially due to high flow velocities and inundation depths. In fact, some of these structures had been designed to withstand tsunami loading. Chock et al (2013) argued that residential light-frame buildings were completely demolished and 75-95% of low-rise buildings in industrial regions collapsed during Tohoku tsunami.

Due to these destructive tsunami events which caused exclusive human casualties and economic loss, the inadequacy of the existing design guidelines for tsunami induced forces was demonstrated (Nistor et al., 2009). Many provisions of these design guidelines were based on effects observed during storm surges and associated flooding. However, tsunami-induced inundation have substantial dissimilarities in terms of their hydrodynamic characteristics and the induced

forces. This study is a part of the ongoing research conducted at the University of Ottawa, Canada, in order to improve the structural design codes for infrastructure located in tsunami-prone areas. Based on FEMA P-646 (2012) classification of tsunami loading, the hydrodynamic force is one of main factors which could cause significant structural damage. Chock et al. (2013) reported substantial structural damage to ocean-facing concrete walls due to extreme hydrodynamic forces due to tsunami waves. These observations vividly outlined the importance of the tsunami-induced hydrodynamic forces for the design of coastal infrastructures. Therefore, serious modifications of the current design codes seem vital.

Different approaches have been carried out to model the tsunami waves' generation, propagation as well as their nearshore transformation and subsequent breaking or surging. The solitary wave is a classical wave generation method used to study the tsunami wave interaction with structures. Numerous studies have employed the solitary wave approach in coastal processes (Synolakis,1987; Ramsden,1993; Liu et al.,1995; Robertson et al., 2011; Linton et al., 2013). Wave generation using dam-break is a newer approach to model tsunami-induced inundation. This is due to the fact that a dam-break wave can produce a highly turbulent hydraulic bore whose characteristics are almost identical to those of typical tsunami broken waves. The experimental generation of dam-break waves can be achieved by the sudden release of the quiescent volume of water impounded into a reservoir over the length of a flume. Due to similar characteristics of dam-break wave to those of tsunami waves, they can properly model the tsunami interaction with inland structures (Chanson, 2006).

Generally, the process of the loading due to tsunami-induced stream-wise forces exerted on structures is divided into four phases, depending on the tsunami-induced inundation characteristics. First, when the bore impacts the structure, an impulsive force occurs (the impact phase). In this stage, significant amount of entrained air bubble mixing in high turbulent bore front results in shock pressure occurring during impact (Bullock et al., 2007). The second phase, which is called transition (reflection) phase, occurs when the reflected bore resulting from the initial impact collapses back and rejoins the incoming bore (Kihara et al., 2015; Linton et al., 2013). The peak force of this phase is more distinct when the bore impacts a vertical wall. Palermo et al. (2013) showed that the generated force (transient force) from this phase is sometimes higher than the impulsive force. In

some cases, a force reduction happens right after transient force due to sudden pressure drop on the upstream side of the column (Bullock et al., 2007). Finally, the quasi-steady phase occurs when both the velocity and bore height contribute to produce maximum hydrodynamic force. At this phase, the pressure distribution is similar to the hydrostatic one and mostly dominant in the total pressure.

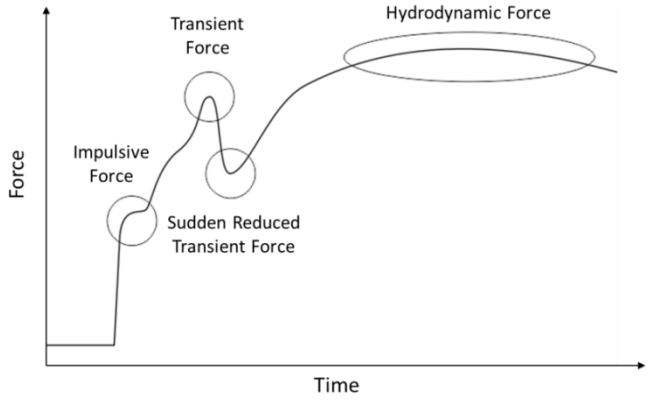

Fig. 1 Schematic of the time history of the stream-wise force exerted on structures for tsunami-induced bores

Many numerical and experimental studies investigated the tsunami bore-structure interaction. Yeh (2007) proposed a new method to determine the tsunami design forces. Lukkunaprasit et al. (2009) verified the aforementioned method employing laboratory experiments based on the same field data and topography in Kamala Beach, Thailand during the 2004 Indian Ocean Tsunami. Ramsden (1993) studied the bore interaction with vertical walls and compared wet and dry bed conditions. Nouri et al. (2010) conducted experimental work to quantify the effect of tsunami-like bores on various types of structural elements. Large-scale experiments were conducted by Kihara et al. (2015) to study the impact of tsunami-like bores on tide walls. They defined three distinct phases (impulsive, reflection and quasi-steady) in the time-history of the pressure exerted on the wall. Robertson et al. (2011) and Linton et al. (2013) conducted full-scale experiments to evaluate hydrodynamic forces impinging vertical walls. St-Germain et al. (2014) investigated the bore-structure interaction using the weakly compressible smoothed particle hydrodynamics (WCSPH) numerical model.

One of the major parameters contributing in the hydrodynamic force equation is the drag coefficient. Currently, available values for the drag coefficients are mostly derived for the steady flow or unsteady flow conditions. Extensive research has been performed in the literature for high Reynolds flow around bluff bodies. Many of them investigated the effects of side ratio of rectangular cylinders on flow characteristics and associated drag coefficient (Sohankar, 2008; Bruno et al., 2010; Tian et al., 2013).

For the case of tsunami bores which behave as unsteady flows (Yeh 2006), there is no clear prescription for the estimation of drag coefficient values. Moreover, these values are attributed to submerged bodies; however, the tsunami bore is in the form of a free-surface unsteady flow. The most relevant laboratory experiments to the present work were performed by Arnason (2005). The author investigated the hydrodynamic force and the associated resistance coefficient induced by the structure-bore interaction. Recently, Shafiei et al. (2016) conducted experiments to determine the maximum stream-wise force and associated drag coefficients for square column with different orientations.

The present paper aims to investigate the variations of the rectangular wall and column aspect ratio (AR=width/depth) and orientation ($\alpha°$) and their effects on the stream-wise force and consequently on the magnitude of the drag coefficients. Square-section structures have been studied extensively in the tsunami literature. However, many rectangular structures are employed in coastal regions. As mentioned in the literature review, many column geometries have not been studied in research papers and there is no recommendation for their drag coefficients in past design codes (such as FEMA-P646, 2012). In the present work, a 3-D numerical model in OpenFOAM was developed to help derive the variation of the drag coefficient generated by tsunami bores for various type of structures. The model is validated using available experimental data for the square column experiment. Subsequently, several different geometry cases, which have not been investigated or cited in the literature, such as walls perpendicular to the flow direction (different AR), elongated rectangular columns in the direction of the flow (different AR) and rotated columns with respect to the flow direction (different $\alpha°$), are modeled numerically. The results of each numerical simulation are discussed in the details and the geometry-dependent drag coefficient is obtained for each case.

2. Description of OpenFOAM

2.1. General Overview

OpenFOAM (Open Field Operation and Manipulation) is a powerful CFD tool for simulating numerous physical phenomena, including coastal engineering problems. OpenFOAM consists of numerous utilities, solvers and libraries, applicable in extensive range of problems. The OpenFOAM source code can be modified for new problems, applications, boundary conditions and solvers. Therefore, it provides a functional approach to solve complicated problems in continuum mechanics.

In the present study, the "interFoam" solver was utilized. This solver is capable of reproducing extreme water and air interactions applicable in free surface and fluid-structure interaction problems. The three-dimensional Navier-Stokes equations (NSE) are solved using the Fnite Volume Method (FMV) discretization for incompressible two phase flow and the Volume of Fluid (VOF) method.

2.2. Governing equations

In this study, the fluid movement is governed by NSEs. These equations describe the conversation of mass and momentum. The fluid is assumed to be incompressible which is a reasonable assumption for practical coastal engineering problems. Pressure and velocity fields are linked in these equations and should be solved simultaneously. The three-dimensional continuity and momentum equations are expressed as (Rusche, 2002)

$$\nabla \cdot \mathbf{U} = 0, \tag{1}$$

$$\frac{\partial \rho \mathbf{U}}{\partial t} + \nabla \cdot (\rho \mathbf{U}\mathbf{U}) = -\nabla P + \nabla . \boldsymbol{\tau} + \rho \mathbf{g} + F \tag{2}$$

where ρ, $\mathbf{U}$ and $\boldsymbol{\tau}$ are the fluid density, velocity vector field and the viscosity stress tensor, respectively. The quantity P, is defined as

$$P = \rho p, \tag{3}$$

where P is the pressure. Furthermore, in (2), F is the momentum source term due to surface tension and can be described as

$$F = \int_{S(t)} \sigma \kappa' \mathbf{n}' \delta(x - x') dS, \tag{4}$$

where σ, κ and **n** are the surface tension coefficient, the surface curvature and the interface normal vector, respectively. Since the fluid in this study is categorized as a Newtonian fluid, the viscosity stress tensor, **τ,** is given by

$$\boldsymbol{\tau} = \mu \, (\nabla \mathbf{U} + \nabla \mathbf{U}^T), \tag{5}$$

where μ is the dynamic viscosity.

2.3. Turbulence model

OpenFOAM provides different methods to simulate turbulent flow motion. One commonly used method in CFD problems is to implement Reynolds-Averaged Navier-Stokes (RANS) equations. In this approach, flow variables ($\emptyset$) represented in NSEs consists of two terms: the time-averaged amount ($\overline{\emptyset}$) and its corresponding fluctuation ($\emptyset'$). Therefore, the equation of $\emptyset$ can be written as

$$\emptyset = \overline{\emptyset} + \emptyset'. \tag{6}$$

By substituting (6) into NSEs, RANS equations can be derived. The additional stress term called Reynolds Stress (R_{ij}) is used in the momentum equation. In order to model the Reynolds stress, the eddy-viscosity concept can be used. Using this concept, all turbulence properties are described as an increased fluid viscosity. The Reynolds stress is defined based on the eddy viscosity and the mean flow strain rate terms as

$$R_{ij} = -\rho \overline{u_i' u_j'} = \mu_t \left(\frac{\partial \bar{u}_i}{\partial x_j} + \frac{\partial \bar{u}_j}{\partial x_i} \right) - \frac{2}{3} \rho k \delta_{ij}. \tag{7}$$

Turbulence models are introduced based on some approximations in the nonlinear terms to obtain a set of closed form equations. Basically, these models are used to determine the eddy viscosity. Moreover, the computational cost is reduced since the number of RANS equations is reduced. One of the most popular turbulence models is standard k-ε model (Launder and Spaulding, 1974) where k denotes the

turbulence kinetic energy and ε denotes the dissipation rate of turbulence energy. Shih et al. (1995) proposed a new turbulence model called as realizable k-ε by adopting an improvement over standard k-ε model. To achieve the correct physical representation of complex turbulent flows, certain mathematical constraints are adopted for the Reynolds stresses. The turbulent viscosity is derived by the equation below,

$$\mu_t = \rho C_\mu \frac{k^2}{\varepsilon} \tag{8}$$

where C_μ=0.09 is considered for the standard k-ε model. This value has been observed in experimental and DNS data for boundary layer and inertial sublayer flow (Shih et al. 1995). To ensure that the model becomes realizable, the term C_μ must be variable rather than a constant and be related to mean strain rate. The following formulation was proposed by Reynolds (1987) and Shih et al. (1994),

$$C_\mu = \frac{1}{A_0 + A_s \frac{Uk}{\varepsilon}} \tag{9}$$

Further information regarding the variables in ((6)) and transport equations for realizable k-ε are presented in Shih et al. (1994) and Shih et al. (1995).

2.4. Volume of fluid model (VOF)

The Volume of Fluid VOF method was initially presented by Hirt and Nichols (1981). This technique is capable of capturing complicated free surface elevations using the volume fraction function. Based on this concept, the interFoam solver employs an indicator function (α) to determine the fractional volume of each mesh cell. Since the application of this study is free surface flow, only water and air are considered here. Therefore, whenever the cell is completely filled with water, the corresponding fraction phase volume is 1 while 0 indicates that the cell is occupied with air. The values between 0 and 1 are representative of cells which represent the free surface. The fluid physical properties can be simply weighted using the VOF method as shown in (10) where the dynamic viscosity, μ, is estimated as

$$\mu = \alpha\mu_{water} + (1-\alpha)\mu_{air} \ . \tag{10}$$

The fluid movement is described by the advection equation; however, Weller (2002) proposed an artificial compression term, $\nabla.\mathbf{U_c}\alpha(1-\alpha)$, in order to improve the interface resolution. Therefore, (10) is re-written as

$$\frac{\partial \alpha}{\partial t} + \nabla.(\mathbf{U}\alpha) + \nabla.\mathbf{U_c}\alpha(1-\alpha) = 0 \ . \tag{11}$$

where $\mathbf{U_c}$ (defined as $\mathbf{U_c} = \mathbf{U_l} - \mathbf{U_g}$) is the relative velocity between liquid ($\mathbf{U_l}$) and gaseous phase ($\mathbf{U_g}$) , representing water and air, respectively. The term **U** in ((6)) is defined as the effective fluid velocity. This velocity is obtained by weighted average of gas and liquid velocities based on their corresponding phase fraction as

$$\mathbf{U} = \alpha\mathbf{U_l} + (1-\alpha)\mathbf{U_g} \tag{12}$$

2.5. Time step control

The self-adapting time step is implemented to ensure that a proper stability of the calculations would be achieved. For this reason, the time step is adjusted using the predefined upper limit values for courant number (Co_{max}) and time step (Δt_{max}). The Courant number is defined as

$$\mathrm{Co} = \frac{\left|U_f.S_f\right|}{d.S_f}\Delta t \tag{13}$$

where d is a vector between the adjacent faces of two control volume. The quantities U_f and Δt in (13) are obtained from the previous time step. Based on these values, the new time step can be measured (Berberović, 2009).

$$\Delta \mathrm{t}^n = \min\left\{\frac{Co_{max}}{Co^0}\ , \left(1+\lambda_1\frac{Co_{max}}{Co^0}\right)\Delta \mathrm{t}^0, \lambda_2\Delta \mathrm{t}^0, \Delta t_{max}\right\} \tag{14}$$

where Co^0 is the value of maximum local courant number. Berberović (2009) suggested that the maximum value of Courant number should not be more than Co_{max}=0.2. The damping factor values $\lambda_1 = 0.1$ and $\lambda_2 = 1.2$ are specified to prevent instability due to time step fluctuation. As long as the maximum local

Courant number does not exceed the limit value, the stability of the time step can be achieved. On the other hand, the intermediate time step (Δt^{*}_{ini}) is specified at the beginning of the simulation to obtain the initial value for time step as

$$\Delta t^{*}_{ini} = \min\left(\frac{Co_{max}}{Co^{0}}\Delta t_{ini}, \Delta t_{max}\right). \quad (15)$$

This intermediate value in (15) as Δt^{0} provides reasonable values for maximum local courant number and subsequent new time step.

3. Model validation

3.1. Physical experiments of Al-Faesly et al. (2012)

The experiments were carried out at the Canadian Hydraulic Center of the National Research Council (NRC-CHC) flume, located in Ottawa. The high discharge flume is 14.56m long, 2.7m wide and 1.4m deep and is constructed from stainless steel (Al-Faesly et al., 2012). The schematic plane layout of the physical experiment is illustrated in Fig. 2. A dam break release mechanism is used in order to generate tsunami-like bores. Based on this method, by suddenly opening a rapidly swinging gate, the water impounded behind the gate is suddenly released and the hydraulic bore advances downstream the flume. The gate opening time ensures and almost instantaneous impounded water release which respected the Lauber and Hager (1998) criterion who demonstrated that the proper duration for the gate opening non-dimensional time should be less than $\sqrt{2}$ in order to create a sudden dam break. According to Al-Faesly (2016), this requirement was met in his experimental setting (maximum non-dimensional time = 0.484).

A vertical drain is located at the downstream end of the flume discharging flow into a lower reservoir. The structural square column model was fabricated using four 6.3-mm-thick acrylic sheets and located at a distance of 4.92m from the swinging gate which ensured that the induced bore was fully developed. The square column with cross section dimension of 0.305x0.305 and a height of1m was installed inside the flume, symmetrically positioned on its longitudinal axis as shown in Fig. 1.

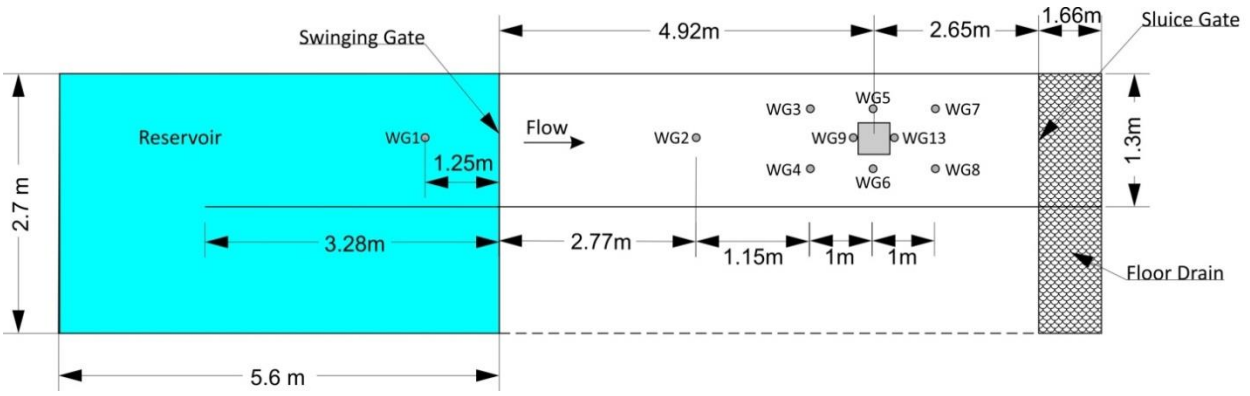

Fig. 2 Plane view of the experimental setting (after Al-Faesly et al., 2012)

In order to measure the bore depth and record its spatial propagation, wave gauges (capacitance-type) were placed inside the flume. Their locations are also indicated in Fig. 2. The hydrodynamic force measurements exerted on the column were conducted by means of a six-degrees-of-freedom dynamometer attached to the column's base. For capturing the pressure, ten pressure transducers (PT), Honeywell 20PC series, were placed vertically along the upstream face of the column.

3.2. Numerical experiments

3.2.1. The Computational Domain

In this section, the experimental results of Al-Faesly et al. (2012) are reproduced using the developed numerical model. The general and initial configuration of the computational domain reproducing the experimental model is shown in Fig. 3. The downstream wall is removed to simulate the presence of the exit drain in the physical flume.

Due to expensive computational cost of using a structured mesh, the domain was modeled using an unstructured grid. Better resolution was chosen near the column because to capture the complexities of the hydrodynamic conditions around it and ensure accurate results in these regions. Therefore, the mesh resolution was refined within a space of 1.5m around the column to capture turbulence effects accurately. The mesh discretization is 1×1×2cm at the column location in x, y and z directions, respectively.

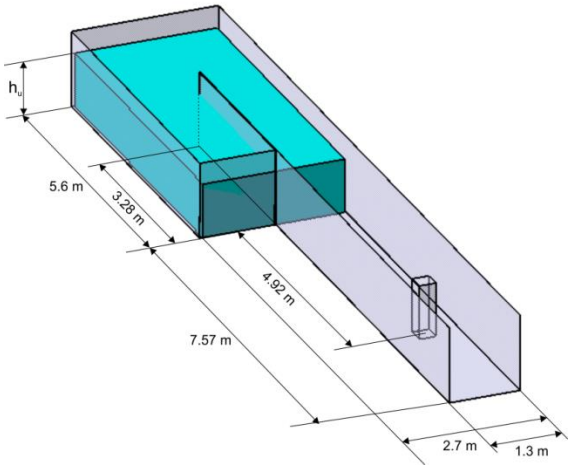

Fig. 3 Computational domain

In *x* direction along the flume length, the mesh resolution starts from 1cm near the column and changes to 4cm, 1.5m away from the column. Mesh cell size was also 1cm in *y* direction along flume width and gradually increased towards the walls, reaching a maximum of 3cm near them. The general mesh discretization size in the *z* (vertical) direction is 2cm which allows the use of the orthogonal mesh. Three impounded water depths (0.55m, 0.85m, 1.15m) were simulated for numerical runs.

3.2.2. Sensitivity Analysis

Sensitivity analyses was performed to assess the influence of various combinations of numerical parameters. Different turbulence models were also used in order to determine the best fit with respect to the accurate reproduction of the results of the physical experiment. Most importantly, turbulence effects on magnitude of the net force exerted on the column, as well as time-history of the free surface water elevation were investigated. Turbulence effects on the time-history of the forces were assessed using the k-ε, k-ω SST (Wilcox et al., 1988), realizable k-ε , Re-Normalized group (RNG) k-ε (Yakhot et al., 1991) turbulence models as shown in Fig. 4. No major difference is observed between the results of these different turbulence models however, the root mean square error (RSME) measurement shows slightly better agreement when using the realizable k-ε model. Moreover, the peak hydrodynamic force obtained using the realizable k-ε model, which occurred around 3.6 sec after the gate opening, follows the same trend and

magnitude as in the case of the experimental results. Also, the impulsive force was only achieved when using the realizable k-ε model. All numerical models show fairly good agreement for the transient force phase, except for the k-ε turbulence model which slightly overestimates the force. Consequently, although all of these numerical simulations demonstrate good agreement relative to experimental results, the realizable k-ε models provides the best match. Therefore, following this sensitivity analysis, all further numerical simulations were performed using realizable k-ε turbulence model.

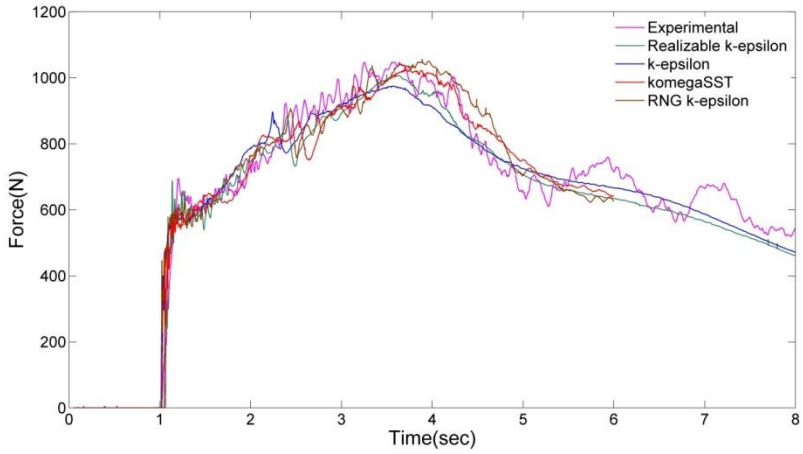

Fig. 4 Sensitivity analysis force time-history results when using various turbulence models

3.3. Comparison of numerical and experimental model results

3.3.1. Water surface elevation

The numerical simulations are compared with the experimental measurements both qualitatively and quantitatively. In order to demonstrate the accuracy of the numerical model results, net stream-wise force and bore surface elevation comparisons with corresponding experimental results are presented in this section. First, the time-history of the free surface elevations are compared for several different wave gauges (WGs) in the absence of the column as shown in Fig. 5. As it can be observed from Fig. 5, although numerical results agree fairly well with the experimental ones, some discrepancies occur for the case of WG1 which is located inside the impoundment reservoir and for the case of WG2 which is located

immediately downstream from the gate. Similar studies by St-Germain (2012) and Douglas and Nistor (2014) also reported the same trend for WG1. The discrepancy augments considerable after 5.0 sec which seems to show that the numerical model performed better for lower water surface levels. This discrepancy is because the water is depleted quicker in the numerical model while the pump remained opened during the experiment.

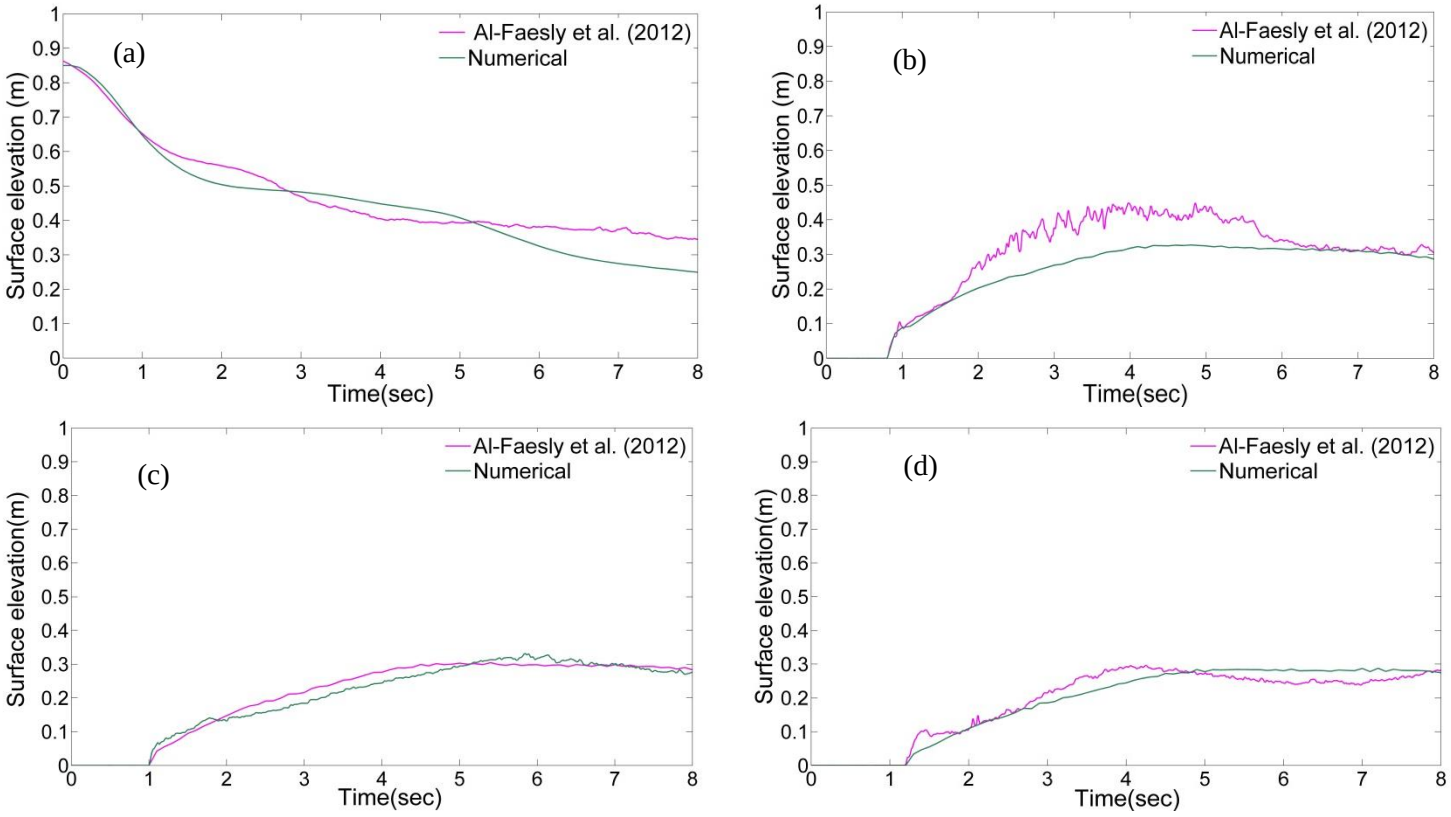

Fig. 5 Water surface temporal variation for $h_u = 0.85m$ a)WG1; b) WG2; c)WG3; d) WG5

Furthermore, the time-history of the water level at WG2 for the experimental test exceeded that obtained by the numerical model. This discrepancy was also reported by St-Germain et al. (2014). Based on the video analysis of the physical experiment, the formation of cross-waves was observed owing to the shock waves induced by gate's fixture at the location of the WG2 (St-Germain et al., 2014). After the bore propagated into the downstream, good agreement in water level

between the numerical simulation and experimental measurements was observed for both the WG3 and WG5 wave gages.

3.3.2. Net stream-wise force

The time histories of the net stream-wise hydrodynamic force exerted on the column in the numerical simulation are shown in Fig. 6. This force was obtained by integrating the pressure exerted on all column faces. The numerically-calculated time-history of the net force shows good agreement with the measured experimental ones. The obtained values of the force for both impulsive and hydrodynamic ones are in good agreement with the experimentally measured data. The results indicate that the numerical model is capable of reproducing the initial impact. Furthermore, after 5.0 seconds , some oscillations can be observed in the wake of the column which is caused by significant turbulence and aeration. Interestingly, for $h_u = 1150$ mm, the transient force did not produce an excessive rise relative to the experiment.

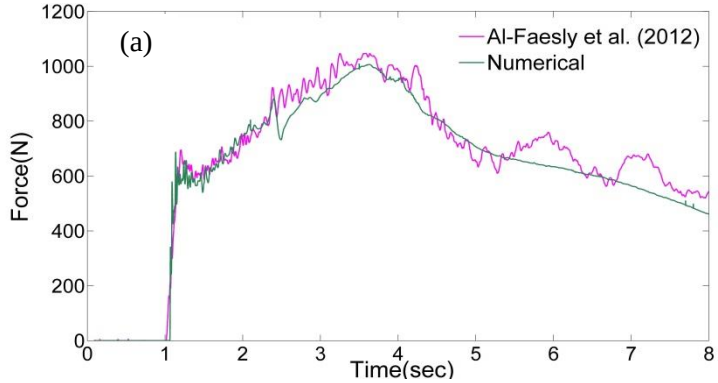

Fig. 6 Time history of stream-wise force exerted on column for $h_u = 1150$mm

4. Drag Coefficient

4.1. Methodology

Larger hydrodynamic forces can cause higher level of damage on structures. This force is also called the drag force in the fluid dynamics and consists of a combination of both pressure and friction drag forces. The friction drag force occurs due to shear stresses caused by motion of the fluid around the structure, while the pressure drag force is generated by the flow pressure exerted directly onto the structure. However, the drag force of the free surface flows differs from

the fully submerged bluff bodies, due to the fact that the hydrostatic pressure is different on the front and lee sides of the structural column. According to FEMA P646 (2012), the equation of the hydrodynamic force can be written as

$$F_D = \frac{1}{2}\, \mathrm{C_d} \rho\, B\, h\, u^2, \tag{9}$$

where $\mathrm{C_d}$, ρ, u, h and B are drag coefficient, fluid density, ambient flow velocity, bore depth and projected width of structure normal to the flow direction, respectively. Gupta and Goyal (1975) studied the flow around the bridge piers for steady flows. They suggested using a term called resistance coefficient ($\mathrm{C_R}$) instead of using the drag coefficient due to the contribution of the hydrostatic force for the free surface flows. Due to the unsteady behavior of tsunami waves, the resistance coefficient is time-dependent rather than a constant coefficient (Arnason 2005).

In order to determine the hydrodynamic force, FEMA P646 (2012) suggests to calculate a term, $(hu^2)_{\max}$, which represents the momentum flux using numerical simulation models. Since the maximum value for both h and u does not occur at the same time (Chock et al., 2016), the temporal variation of the momentum flux value (hu^2) should be measured to calculate the hydrodynamic force accurately. In addition, the grid size at the run-up zones should be fine enough to ensure the accuracy of the simulations. Finally, reverse calculation is used to compute the drag coefficient ($\mathrm{C_d}$) using the numerical results such as net stream-wise hydrodynamic force (F), the bore depth (h) and the flow velocity (u). In order to measure the drag coefficient, both the bore depth (h) and flow velocity (u) are taken from the unobstructed flow condition, without the presence of the structure in the flow field (Yeh, 2007). Therefore, all numerical simulations are initially performed for the no-obstruction condition and for different impounded water depth to measure the temporal variation of the hu^2 term at the structure's location. It is worth mentioning that in the present work, the drag coefficient is equivalent to the resistance coefficient since the force obtained from numerical results contains both the hydrodynamic and hydrostatic force components.

4.2. Effect of sidewalls/constrictions

In order to assure the analogy between the numerical model and the prototype, the Froude number equivalence for free surface flows is ensured. The effects of sidewalls, which occur both in the numerical and physical models, can cause

significant discrepancies between the numerical simulations and the real-size prototype. The effect of sidewalls can be investigated using the blockage ratio (BR= structure width/flume width). The numerical domain is scaled up using this ratio to eliminate the influence of sidewalls on the net stream-wise force and other bore characteristics. To assess how the sidewalls affect the bore-structure interaction, the flume width is increased and the time histories of the force exerted on the column are compared for different blockage ratios (Fig. 7). The flume width was increased until no significant difference was observed in the measured forces exerted on the column in the numerical simulations.

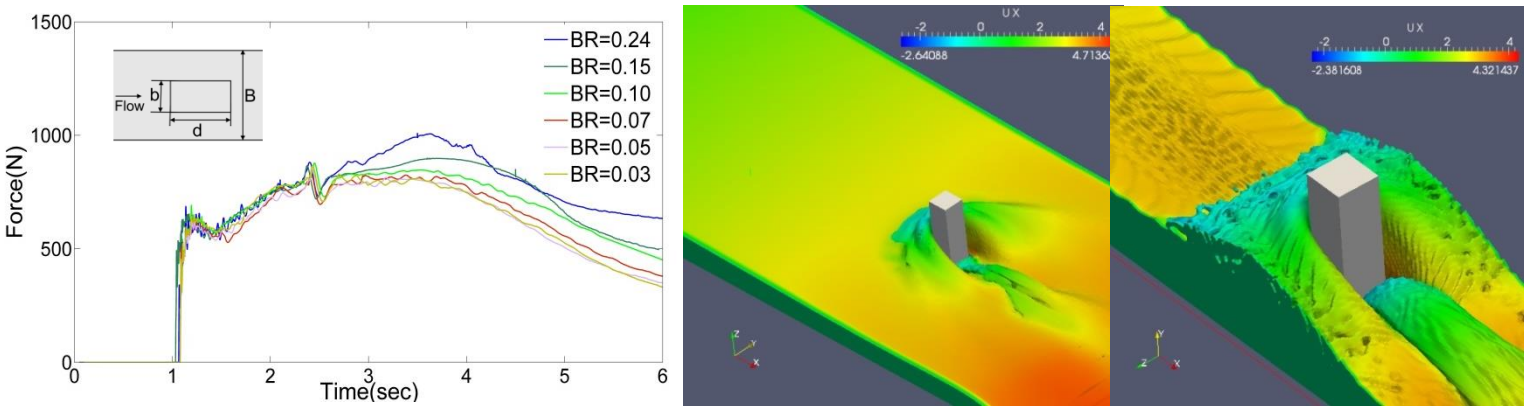

Fig. 7 Influence of blockage ratio on time history of stream-wise force (right) and qualitative comparison of the bore surface elevation for BR=0.24(middle) and BR=0.07(left)

As illustrated in Fig. 7, the maximum difference between blockage ratios was less than 7 percent. As the bore impinges onto the column, the run-up height increases and then it collapses back onto the incoming bore and consequently forms a front-face surface-roller. This surface-roller propagates then into the upstream-side and toward the sidewalls. For a narrower flume (lower blockage ratio), the surface-roller is reflected by the side wall and causes a subsequent water level build-up in front of the upstream face. Fig. 7 illustrates the qualitative comparisons of the water surface elevations on the upstream side of the flume. For the case of BR=0.07, the surface-roller dissipated before reaching the sidewalls: therefore no water accumulation occurred in front of the upstream side. St-Germain et al. (2014) doubled the flume width in their SPH numerical model to examine the effects of the sidewall and they also observed that both the bore net stream-wise force and run-up elevation reduced during the hydrodynamic (quasi-steady) phase as a results of increasing the width of the flume. It should be noted that the

occurrence of hydrodynamic force peak for higher blockage ratios occurs when the water surface elevation rise at the upstream side while for higher blockage ratios, the quasi-steady phase is almost constant. Arnason (2009) also observed the formation of bow wave (surface-roller) during the maximum hydrodynamic force peak and presumed that both critical flow condition and sidewall effects caused the aforementioned phenomenon.

5. Results and Discussion

5.1. Influence of structure's geometry

In this section, the effects of the structure's geometry on the hydrodynamic force and the associate drag coefficients are investigated. The impact of bores on columns with different geometries, such as square or rectangular, were modeled numerically for different aspect ratios and orientations. The schematic views of the computational domains for the aforementioned columns are presented in Fig. 8. The blockage ratio (BR) was kept as 0.07 for all the simulations to eliminate the wall effects (Section 4.2). For the rectangular-section columns, the numerical simulations were performed for the selected aspect ratios, AR, of 1,2,4,6,8 while for the rectangular-section walls, the aspect ratios, AR, of 2,4 were considered. The reference cross-section is a square column with dimensions of 0.305m×0.305m. In order to investigate the column orientation (α) effects, the square column was rotated about its axial axis by 0°, 22.5°, 45° and 67.5° with respect to the direction of the bore flow. Finally, the rectangular-section columns with AR of 1:4 and the orientation angles 22.5°, 45° were simulated numerically.

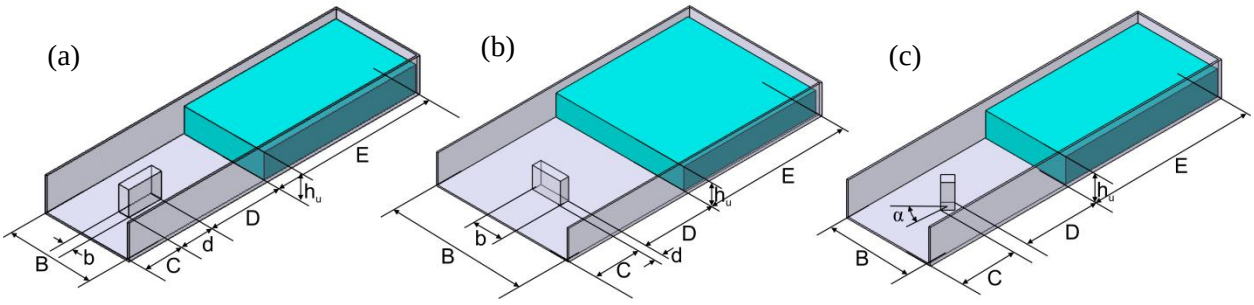

Fig. 8 Structural geometry variation a) elongated column b) rectangular wall c) rotated square column, $E = 8.6m, D = 4.75m, C = 2.5m,$ AR=b/d, α=0°,22.5°, 45°.

5.2. Influence of aspect ratios for rectangular columns

5.2.1. Net stream-wise hydrodynamic force

The hydrodynamic effects caused by the presence of the elongated columns in the flow direction are presented in this section. The numerical simulations are performed for impounded water depths (h_u) of $1000mm, 850mm$ and $550mm$. The time-histories of the net stream-wise hydrodynamic force are presented in Fig. 9 for two impoundment depths, $\mathrm{h_u} = 1000\mathrm{mm}$ and $\mathrm{h_u} = 550\mathrm{mm}$. The initial impact force has almost the same magnitude for all aspect ratios of the structural elements. This trend is similar for all aspect ratios owing to using the same distance from the gate and same geometry of the upstream face exposed to the hydraulic bore. As illustrated in Fig. 9, the total force exerted on column slightly increases by elongating the column in the flow direction. On the other hand, for all impounded water depths, the hydrodynamic force occurring at the quasi-steady state phase shows a constant variation. According to Arnason (2009), the influence of flume sidewalls leads to additional water level built-up at the upstream face and a subsequent higher bore level. This generates a distinctive force peak during the quasi-steady force. This force peak is not observed in the current study which shows that the influence of wall was properly eliminated.

Moreover, for all adapted initial impounded water depths, the value of the transient and hydrodynamic quasi-steady forces overshoot that of the impulsive force. For the impoundment depth $\mathrm{h_u} = 550\mathrm{mm}$, the initial impulsive force is less than 50% of subsequent hydrodynamic force. This supports Arnason's (2005) conclusions which indicated that the magnitude of the initial impact force was less than of the quasi-steady force for impounded water depths larger than 200 mm. Conversely, for impounded water depths of less than 200mm, the magnitude of the initial impact force was in fact larger. In addition, only for this impounded water, the transient force is slightly less than the later observed quasi-steady hydrodynamic force. It should be noted that for lower initial impounded depth, the transient and impulsive forces were not distinguishable in Arnason's (2005) study. As illustrated in Fig. 9, at around 2.3 sec, a momentarily distinct rise occurs in the time-history of the force for all simulations. This rise is attributed to the transient force occurring at the reflection phase. Moreover, it can be observed from Fig. 9 that, by

increasing the aspect ratio of the column, the magnitude of the hydrodynamic force slightly increases as well.

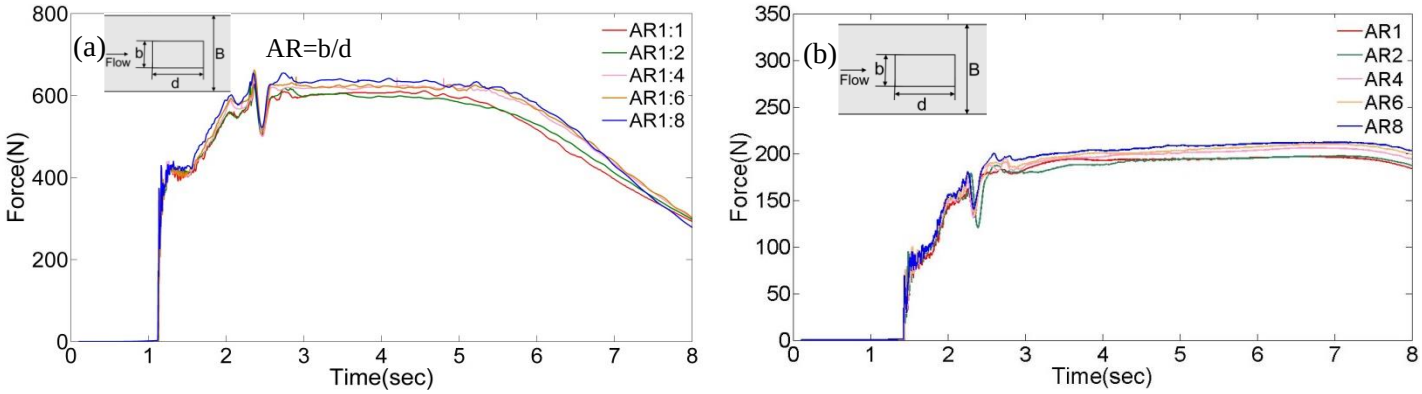

Fig. 9 Time history of net stream-wise hydrodynamic force for different impounded water for column with AR1, AR2 , AR4, AR6 and AR8 a) 1000mm b)550mm

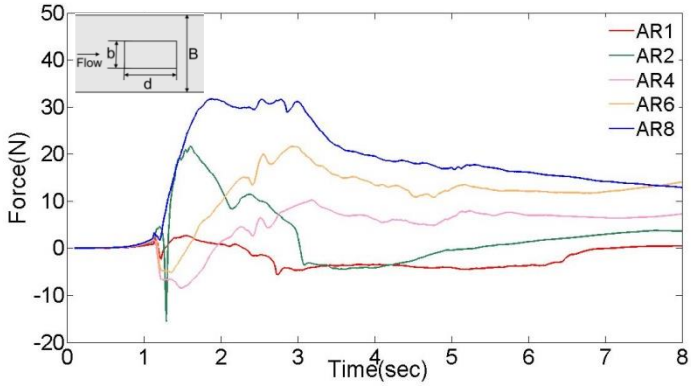

Fig. 10 Time histories of the friction drag forces for columns with AR1, AR2, AR4, AR6 and AR8 for 1000mm impounded water

This rise is due to the increase in both the shear force on column sides as well as the pressure difference between the upstream and the leeside of the column. The constant gradual increase in the total net stream-wise force appears shortly after the initial impact at 1.2 sec. This difference can be seen in Fig. 10 which shows time history of the friction force variation exerted on column sides. However, this increase in total stream-wise force is not a considerable as the aspect ratios increase. As shown in Fig. 9, the maximum difference in the total stream-wise

hydrodynamic force between AR1:1 and AR1:8 is 8% during the quasi-hydrodynamic phase. The general trend indicates that the aspect ratio increase leads to increase in the shear stress on the side walls of the column. However, the friction force induced by the shear stresses has a small contribution to the total magnitude of the stream-wise hydrodynamic force. The comparison between Fig. 9 and Fig. 10 shows that shear force (Fig. 10) contributes less than 5% in the total stream-wise hydrodynamic force for the numerical simulation of AR1:8.

A similar low contribution of the shear stress is also reported in Wu (2004) and Lin and Li (2003). Wu (2004) obtained the same results for the dam break wave problem hitting a square column by implementing both LES and k-ε turbulence models. He concluded that the contribution of the shear stress is less than 1% which he judged to be negligible. As shown in Fig. 10, a dip occurred at the first moments of the simulations. This is attributed to the recirculation regions which occurred downstream of the separation points as the flow splits due to sharp leading edge as shown in Fig. 10. The 2-D flow features around the column are presented in Fig. 11 to point out some of the main hydrodynamic characteristics that are responsible for the drag force and pressure variation. Shortly after the dip, the positive force starts to grow due to the flow reattachment. This reattachment region can be visualized alongside the column's sidewalls, downstream of the separation vortices. Since pressure distributions show similar trends for all tested aspect ratios, for simplicity, only the streamlines for AR1:4 and AR1:8 columns at the location of 10cm above the channel bottom are presented and compared here. The flows extend to downstream about the column width and eventually rejoin in the wake. This forms vortices in the wake of the column which causes the low pressure region at leeside of the column. This low pressure region persists around 6.0 sec during the quasi-steady state phase until the reversed flow started to fill the column leeside. However, as can be observed in Fig. 11, the water level and subsequent pressure values at the column's leeside are still negligible. As a consequence, an almost constant and substantial pressure difference was obtained. Eventually, the increased shear and pressure variations cooperate and result in an increase in the total net stream-wise forces exerted on the column.

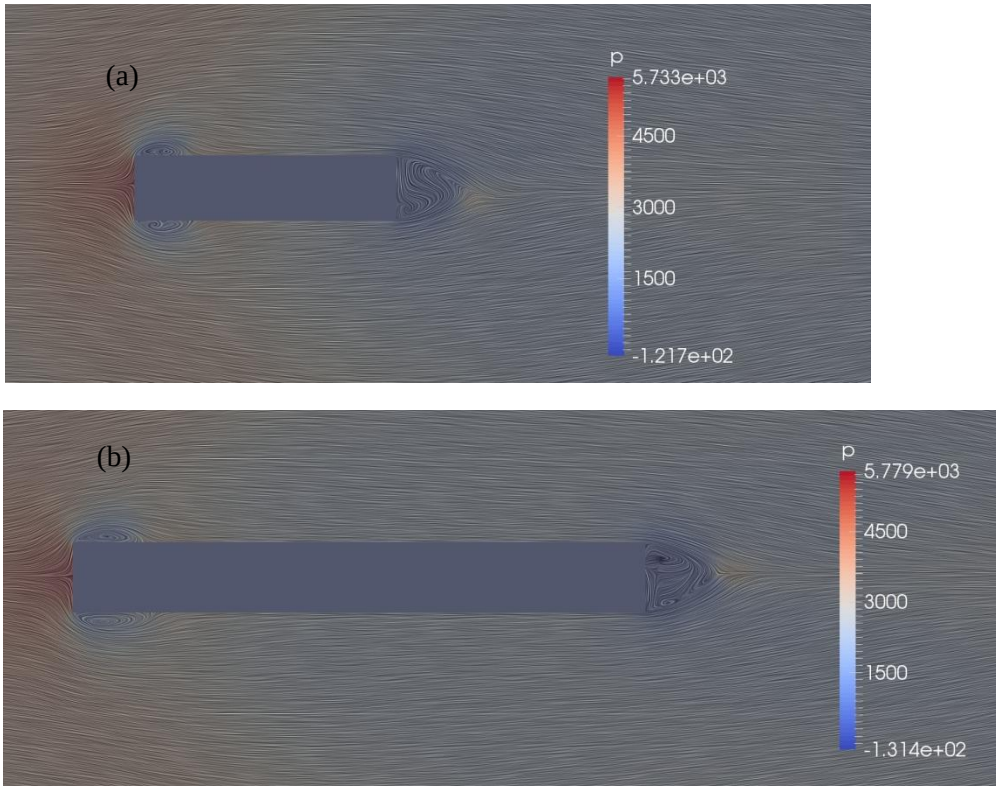

Fig. 11 Pressure field and streamlines 6.0sec after initial impact along the column with two aspect ratios a) AR4 and b) AR8

Generally, as the distance from the flume bottom increases, the pressure decreases. The contribution of the dynamic pressure in the total pressure is considerable at the first moments of impact and after that, the hydrostatic pressure is mostly dominant.

As the bore impacts the column, separation occurs due to square column sharp edges. Therefore, the incoming bore splits into two streams reaching farther at the downstream side. After the bores converge in the wake of the structure, the so-called "rooster tail" with triangular shape forms. As shown in Fig. 12, comparisons of bore evolution around the column at several key moments are presented. After 2.1 sec from initial impact, for both AR's, the bore converged in the wake of the structure and formed the rooster tail. This type of high turbulent bore at this area was also observed during experimental tests (Arnason et al. 2009, Nouri et al. 2010). However, as displayed in Fig. 12, the rooster tail developed in the wake of AR1:1 merged earlier than that occurring for the AR1:8 case. The width of the formed rooster tail is approximately equal to the structure's width for both AR's: however, its length is longer for the case of AR1:8. After 6.0 sec from initial impact, the bore merged and filled the column leeside for AR1:1 but for

AR1:8 the bore didn't reach the leeside yet and the stagnation areas are distinct as the velocity is still low and the column leeside is almost dry (Fig. 12b and 12d).

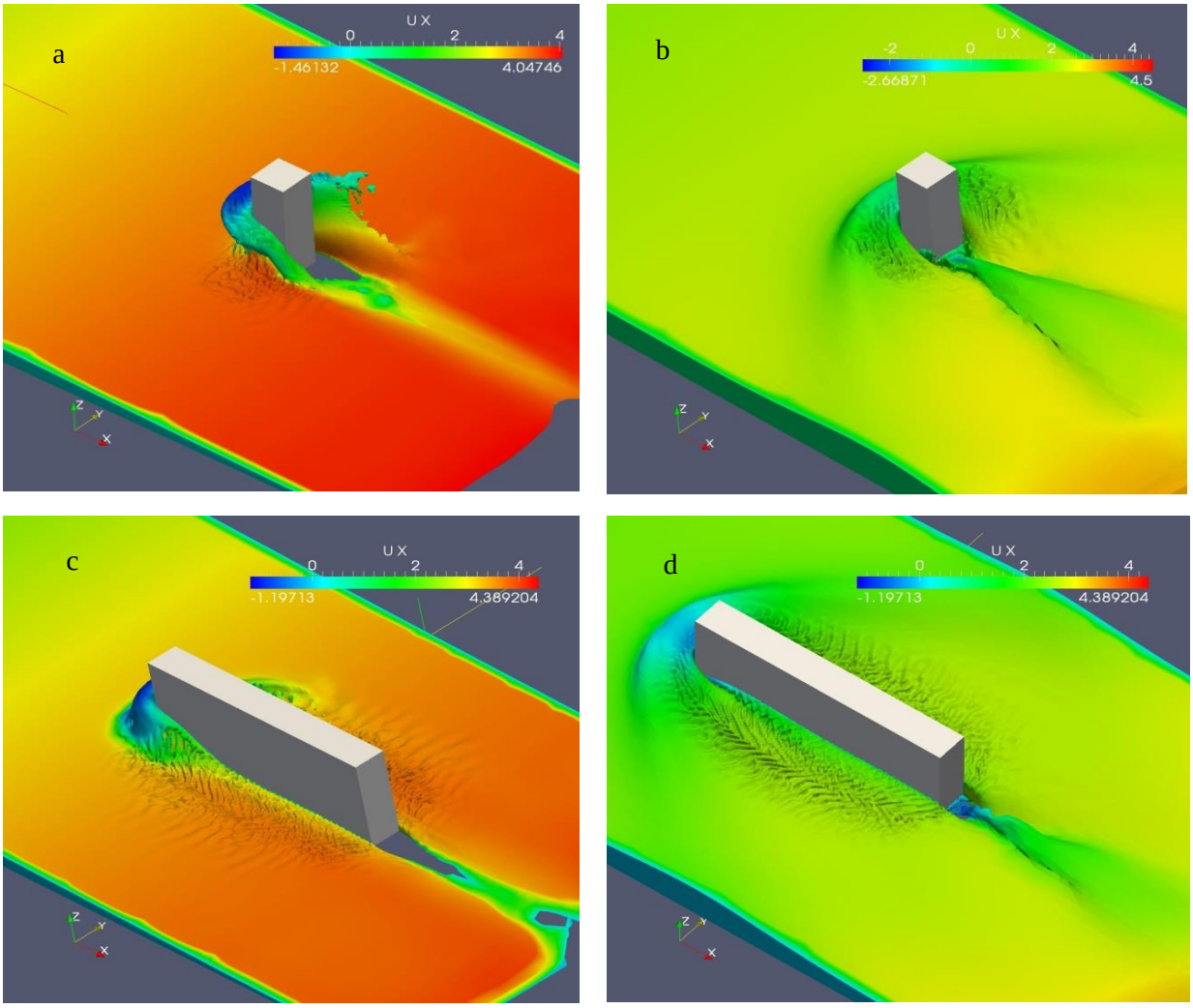

Fig. 12 Formation of rooster tail for AR1:1 at the following instants after initial impact: a) 2.1sec b) 6.0sec AR1:8 c) 2.1sec d) 6.0sec

Therefore, as shown in Fig. 12, the pressure at the leeside of the AR1:8 column is close to zero. However, the value of pressure at the AR1:1 leeside is 1.5kPa and is almost negligible with respect to the total pressure. Therefore, it would not contribute to any considerable change in pressure difference. Overall, based on these observations, neither contributing factors (pressure difference and friction drag) had substantial effects on increasing the bore stream-wise hydrodynamic force by increasing AR. As a result, for the tested AR's ranging from AR1:1 to AR1:8, a slight rise in the net stream-wise hydrodynamic force was obtained.

Moreover, time-histories of the drag coefficient variation for elongated columns with different aspect ratios was investigated. The cases for impoundment depths of $h_u = 550mm$ and $h_u = 1000mm$ are presented in Fig. 13. For all aspect ratios, the time histories of the drag coefficient follow similar trends. After the initial impact, the trend is almost similar for all cases.

It is also evident that C_d gradually decreases with an increase in the impounded water depth. The same trend was also reported by Arnason (2005). Furthermore, for different cases of aspect ratio, since the hydrodynamic force increases, C_d also increases which results in a marginally higher aspect ratio.

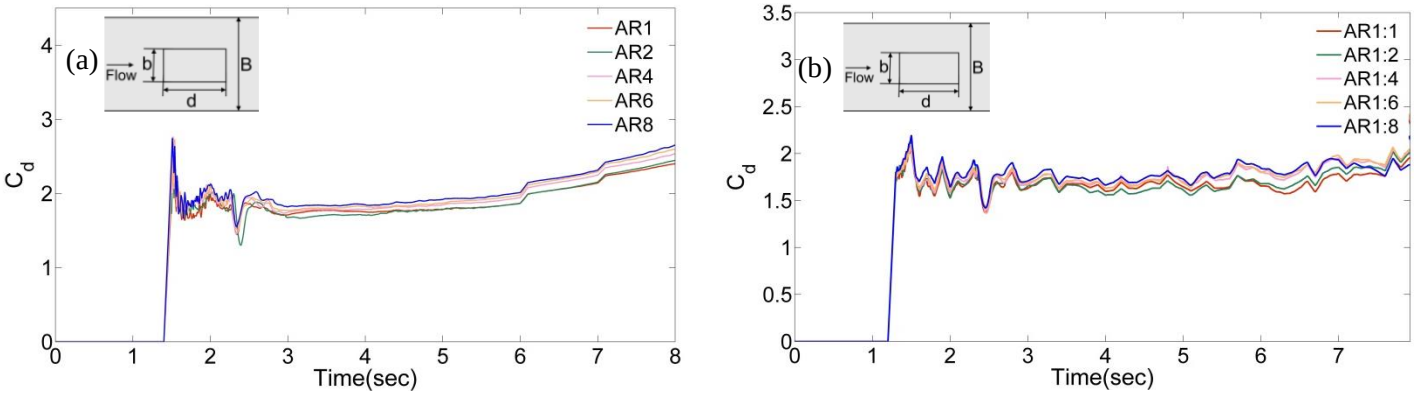

Fig. 13 Time-history of drag Coefficient for two impounded water depths: a) 550mm b) 1000mm

5.3. Rectangular walls with different aspect ratios

The effects of a tsunami bore with a rectangular wall is different that rectangular columns. The bore impact generates larger hydrodynamic forces as the column width normal to the direction of flow increase. In addition, most research work conducted on the impact of the tsunami bore with rectangular walls, measured significant values of transient force during the reflection phase (Kihara et al. 2015, Linton et al., 2013). Therefore, the associating drag coefficient induced by a rectangular wall could be affected and should be taken into careful consideration.

For this reason, rectangular walls with AR2:1 and AR4:1 were also examined and the results are presented in this section. Two impounded water depths, $h_u = 550mm$ and $h_u = 1000mm$, were selected to investigate these cases.

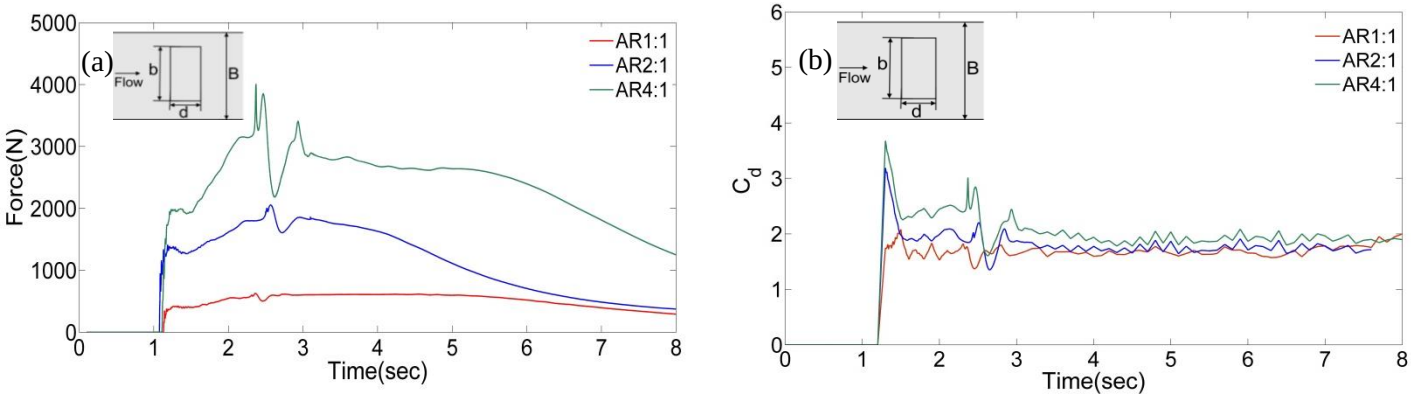

Fig. 14 Rectangular-section walls with different aspect ratios a) Time-history of net stream-wise force for $h_u = 1000$mm b) Time-history of Drag Coefficient for $h_u = 1000$mm

The subsequent hydrodynamic force and the drag coefficient were then estimated using the similar scaled up domain with BR = 0.07. Fig. 14 shows the net stream-wise hydrodynamic force and the associated drag coefficient time-histories for the square cross section and for the sections with AR2:1 and AR4:1 sections for the impoundment depth $h_u = 1000$mm.

The overall trend indicates that the hydrodynamic force is increased by 40% between the sections with AR2:1 to AR4:1. As shown in Fig. 14a, four distinct sections appear in the resulting force time histories including impulsive force, transient force peak, reduction in transient force and hydrodynamic force.

In addition, another significant reduction in hydrodynamic force can be observed following the transient force peak. This can be attributed to the corresponding low pressures which mostly occur when the entrapped air is compressed during impact (Bullock et al., 2007). The reduction in the transient force is less than 50% of the peak transient one. As shown in Fig. 14a, the transient force occurred around 2.3 sec after initial impact and overshoots significantly the subsequent quasi-steady hydrodynamic force. This was also observed in Linton et al.'s (2013) experimental work. The authors reported that the value of the transient force was 2.2 times larger than the mean hydrodynamic force. In the current study, the ratio of peak transient force to subsequent mean hydrodynamic force was found to be less than 1.45.

The wall was extended through the whole width of the channel in Linton et al.'s (2013) work; therefore, the reflection process was more intense and associated with higher turbulence effects. However, in the present study, a portion of the flow

was reflected and fell back onto the incoming bore after the initial impact while the remaining portion flew downstream around the wall. This difference during reflection phase leads to discrepancies in the resulting transient forces.

5.4. Influence of orientation for square and rectangular columns

5.4.1. Net stream-wise force

In this section, the effects of different structural orientation with respect to its original alignment (α) on the net stream-wise hydrodynamic force is investigated. Further, the drag coefficient is computed for each orientation. The time history of net stream-wise force exerted on the square column with different orientation is presented in Fig. 15a for the case of an impoundment depth, $h_u = 1000\text{mm}$. For $\alpha = 22.5^\circ$ and $\alpha = 67.5°$ orientations, the evolution of the time histories of the hydrodynamic force is almost identical. As it can be observed from Fig. 15, the values of the impulsive and hydrodynamic forces vary depending on the structure orientation with respect to its initial alignment ($\alpha = 0°$). The impulsive force, which occurred around 1.2 sec, had lower values with an increase in the structure orientation. For the case of $\alpha = 0^\circ$, the impulsive force increased about 36% relative to the case of $\alpha = 45°$.

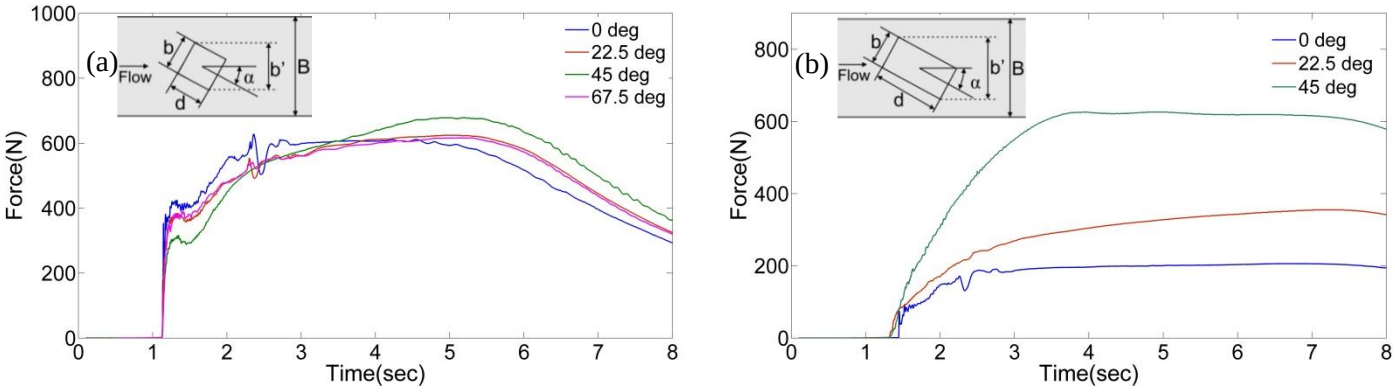

Fig. 15 Time-history of net stream-wise hydrodynamic force for columns with different orientation a) Square for an impoundment depth $h_u = 1000\text{mm}$ b) Rectangular for an impoundment depth of $h_u = 550\text{mm}$

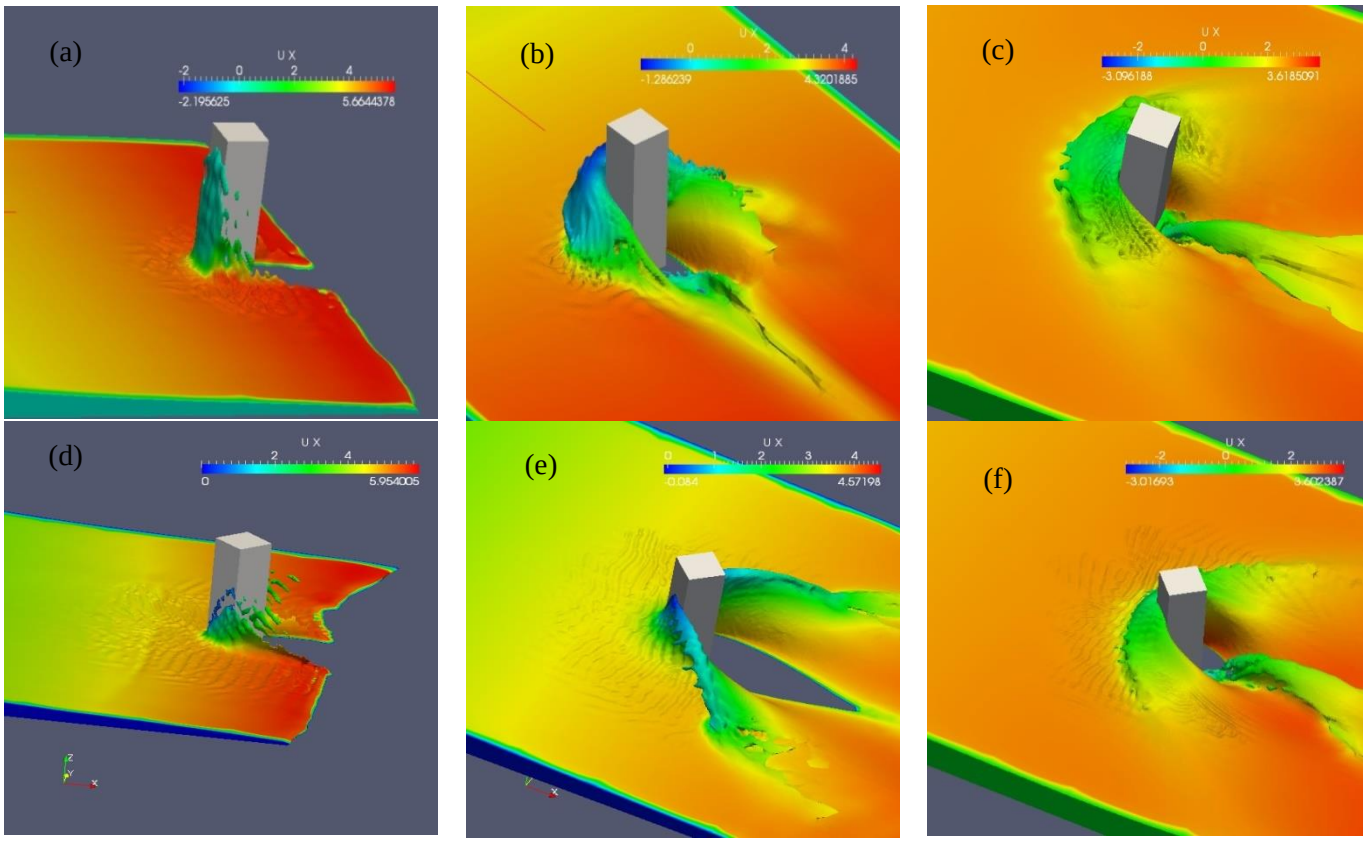

Fig. 16 Free water surface a initial impact and during transient phases for impact on a square with structure orientations of α= 0° at a) t=1.3sec b) t=2.3sec c)t=5.0sec and α= 45° at d) t=1.3sec e) t=2.3sec f)t=5.0sec

This change occurred due to the sharp edge of column for the case $\alpha = 0^\circ$ when facing the incoming bore. For the case of $\alpha = 45°$, the lowest impulsive force occurred since the corner edge of the square column faces the flows. Therefore, flow moved around the column more smoothly. The transient force occurred after 2.3 s, showing greater values for the case when $\alpha = 0^\circ$ because the water level rose at the upstream side of the column. This did not occur for $\alpha = 45°$ as bore passed around the column with no observation of water build-up on the upstream side of column. On the other hand, the maximum hydrodynamic force occurred for the particular structure orientation angle $\alpha = 45°$. This is because by rotating the column, the projected width (b' in Fig. 15) to the flow direction increases (it becomes in fact the diagonal of the cross section) and, consequently, the hydrodynamic force increases. For case $\alpha = 22.5°$ (α=67.5°), the maximum value of the hydrodynamic force is slightly greater than $\alpha = 0°$ as b' is slightly higher. In

other words, the resultant pressure exerted on the two faces of $\alpha = 45°$ orientation frontally facing the incoming flow is larger than the pressure exerted on the upstream face of the square column.

To better understand the variations of resulting force, qualitative comparisons of water surface at some key moments are presented in Fig. 16. In this figure, water surface profiles are illustrated during the impact, transient, and quasi-steady phase for cases with $\alpha = 0°$ and $\alpha = 45°$. In Fig. 16a, the bore run-up on the upstream face of the column can be clearly observed; however, in Fig. 16c, no run-up can be observed as the flow is directed into two streams moving by the corner edge facing the incoming bore. Further, during the transient phase (Fig. 16b and Fig. 16e), the difference between the cases $\alpha = 0^\circ$ and $\alpha = 45°$ is noticeable. The surface-roller is formed by the bore reflection from the upstream side of the column for the case $\alpha = 0^\circ$ and leads to an increase in the water surface level in front of the upstream face, leading thus to a larger hydrodynamic force relative to the case with $\alpha = 45°$. For the case with $\alpha = 45°$ (Fig. 16e), the formed rooster tail is higher in length compared to $\alpha = 0°$ orientation (Fig. 16b). Fig. 16c and 16f indicate that the pressure difference after 5.0sec is also higher for $\alpha = 45°$ orientation as the column leeside is steel dry.

Similar results were obtained by Shafiei et al.'s (2016) experimental work. They investigated the structure orientation influence on the resulting force exerted on the square column with orientations $\alpha = 0^\circ$, $\alpha = 30^\circ$ and $\alpha = 45°$. The highest initial impact force and hydrodynamic force obtained by their experimental works for $\alpha = 0^\circ$ and $\alpha = 45^\circ$, respectively. Arnason (2005) also reported higher hydrodynamic force for the case of $\alpha = 45^\circ$ with the ratio less than $\sqrt{2}$ comparing with the case $\alpha = 0°$.

The time histories of the drag coefficient for all structure orientations are presented in Fig. 17. As shown in this figure, the $\alpha = 0°$ orientation leads to the largest magnitudes of drag coefficient for both the square and the AR1:4 columns. Based on these observations, using drag coefficient values corresponding to the $\alpha = 0°$orientation appears conservative for design considerations.

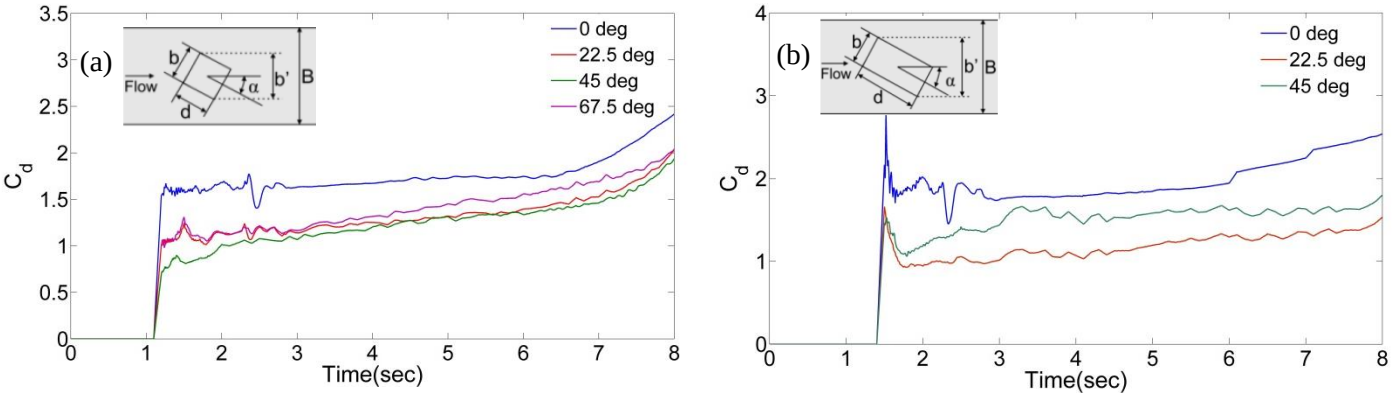

Fig. 17 Time history of the drag coefficient for the square column with different orientations a) $h_u = 1000mm$ b) $h_u = 550mm$

5.5. Drag Coefficient

The variation of the drag coefficient, $C_{d,}$ with respect to the aspect ratio, AR, and the flow depth, h_u, is presented in Table.1. The comparison between the values corresponding to aspect ratios AR1:1 to AR1:8 shows that C_d values increase about approximately 0.12 with a decrease of 0.45 m in the impounded water depth. The *mean* drag coefficient was calculated as an average value over the period of time between the initial impact and the moment when the reservoir is close to depletion. This instant occurred regularly after approximately 6.0 sec. The mean C_d varied between 1.68 to 1.91 for all impounded water depths and aspect ratios. These results are also similar to those of Arnason's (2005) for his C_d values with average values ranging from 1.99 to 2.26 for the square column for tested impoundment depth, h_u, between 100mm to 300mm. The results also show that the value of C_d=2.0 adopted by FEMA P646 (2012) for the square column and the elongated column at this examined range (AR1:1 to AR1:8) is appropriate.

For rectangular walls, the drag coefficients were estimated and presented in Table 1. Unlike the rectangular columns, C_d increases with an increasing h_u. The mean C_d for aspect ratios AR2:1 and AR4:1 walls are 1.8 and 2.05, respectively. As demonstrated by the time histories of the drag coefficient in Fig. 14b, values of C_d during the reflection phase were 2.2 and 3.0 for the AR2:1 and AR4:1 walls respectively and for $h_u = 1000mm$.

On the other hand, for square columns with different orientations, the value of C_d decreased as the orientation angle increased (Table 2). The lowest value of C_d was obtained for $\alpha = 45$. Similar to rectangular section columns with varying AR, higher values of C_d were observed when increasing h_u. Shafiei et al. (2016) observed the same trend in their experimental results. They reported C_d values of 1.15, 1.40 and 1.65 for orientations of $\alpha = 0$, $\alpha = 30^\circ$ and $\alpha = 45°$, respectively. However, for their obtained C_d values, the contribution of the hydrostatic force was excluded. Moreover, their drag coefficient values were obtained for a bore depth of 210mm at the location of the structure which differs from examined impounded water depth in the present study.

Table 1 Drag coefficient values for different impounded depths and for rectangular column with different aspect ratios

Aspect ratio AR	Impoundment depth $h_u = 1.0$ m	Impoundment depth $h_u = 0.85$ m	Impoundment depth $h_u = 0.55$ m
Square	1.68	1.74	1.80
AR1:2	1.67	1.72	1.78
AR1:4	1.72	1.80	1.84
AR1:6	1.74	1.83	1.87
AR1:8	1.77	1.87	1.91
AR 2:1	1.80	-	1.70
AR 4:1	2.05	-	1.92

Table 2 Drag coefficient values for different impounded depths and for square column with various orientations

Orientation (α)	Impoundment depth ($h_u = 1.0$ m)	Impoundment depth ($h_u = 0.85$ m)
Square (α=0°)	1.68	1.74
Square (α=22.5°)	1.37	1.30
Square (α=45°)	1.32	1.24
Square (α=67.5°)	1.41	-

Table 3 Drag coefficient values for different impounded depths and for rectangular column with AR1:4 with various orientations

Orientation (α)	Impoundment depth ($h_u = 1.0$ m)	Impoundment depth
AR1:4 (α=0°)	1.72	1.84
AR1:4 (α=22.5°)	1.14	1.12
AR1:4 (α=45°)	1.47	1.49

Furthermore, Arnason (2005) reported C_d values ranging from 1.72 to 2.22 for the case of $\alpha = 45°$. These aforementioned values for C_d are consistent with the present work as higher values of C_d are expected with an increasing h_u. On the other hand, the drag coefficient obtained for the case of the rotated column with AR1:4 ($\alpha = 22.5°$ and $\alpha = 45^\circ$) were also presented (Table 3). Interestingly, lower values of C_d were obtained for these cases compared to the AR1:4 with $\alpha = 0^\circ$ orientation. It seems that the values of C_d obtained for $\alpha = 0°$ orientation were dominant and could conservatively be considered for design of structure located in tsunami-prone areas.

In Fig. 18, the estimated values in the present work are compared with results from Arnason's (2005) experimental study. One can noticed that an increase in the impounded water depth (h_u) leads to a decrease in the magnitude of the drag coefficient (C_d). The values of the drag coefficient for rectangular and also square columns with various orientations are also plotted in this figure. These values of C_d are close to the regression lines obtained from results plotted for the square with $\alpha = 0^\circ$ and $\alpha = 45°$ orientations.

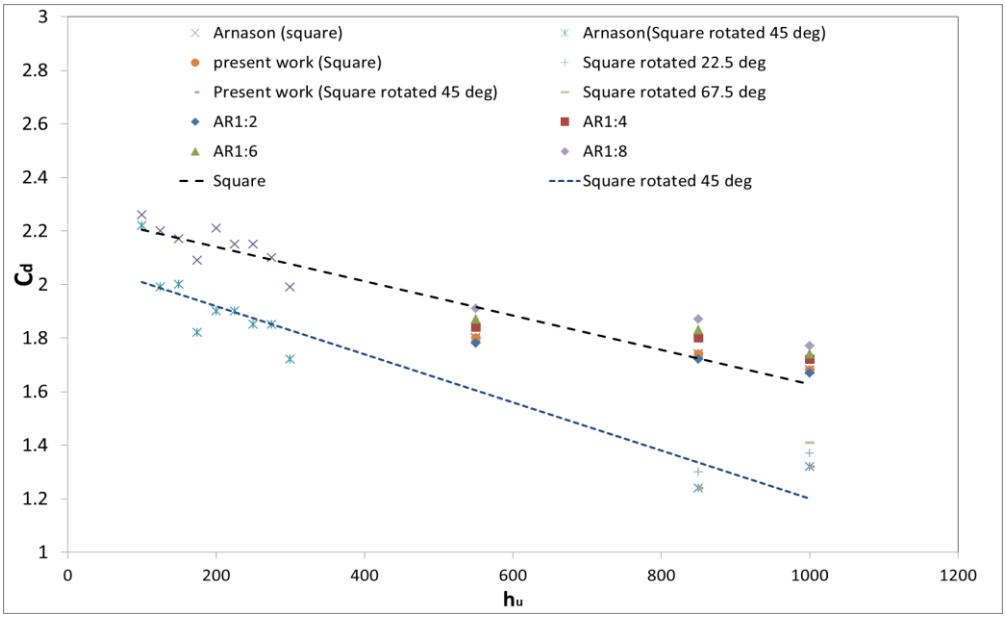

Fig. 18 Variation of the drag coefficient, C_d versus the impounded water depth (h_u)

6. Conclusions

In the present study, the interaction between rectangular cross-section structures with different aspect ratios and orientations with respect to the direction of the tsunami-like bores were investigated with the purpose of investigating the associated drag coefficients. Based on previously demonstrated literature results, the dam-break wave analogy with tsunami-like bores was employed and a three-dimensional numerical model implemented in OpenFOAM was developed. First, the numerical model (based on the RANS equations with the realizable k-ε turbulence model) was validated using experimental results of physical experiments conducted at NRC-CHC in Ottawa, Canada. In order to eliminate the side wall effects of the numerical simulations on the results, a scaled-up domain was selected using a proper blockage ratio. Then, several dam-break simulations impacting rectangular cross-section columns with various aspect ratios (AR= 1,2,4,6 and 8) and walls (AR=2 and 4) were further conducted. The effects of structural orientations ($\alpha = 0^\circ$, 22.5° and 45°) were also investigated for square cross-section columns (AR1:1) and AR1:4. The drag coefficients for each case study were derived using the calculated time-histories of the stream-wise forces, water surface elevations and flow velocities.

One of the most recent documents which provides guidelines for the design of structures in tsunami-prone areas, FEMA P646 (2012), suggests a uniform drag coefficient value for the square cross-section columns ($C_d = 2$) and does not provide any information for elongated or columns rotated with respect to the incoming flow. The present study provides an in-depth investigation on the drag coefficients for elongated and rotated structures. The mean drag coefficient range for rectangular-section column with (AR= 1,2,4,6 and 8) was found to vary from 1.68 and 1.91. It was observed that, as the aspect ratio increased, the resulting mean drag coefficients also increased. Lower values of the drag coefficients were obtained when using higher bore depths. For rectangular section walls (AR=2 and 4), the drag coefficients varied from 1.7 to 2.05. During the reflection phase (run-up splash), higher values of the drag coefficients were observed and the authors hence recommend that they be considered in the design process. In addition to the effect of the wall geometry in terms of its aspect ratio, on the drag coefficients, the numerical simulations showed that using higher bore depths resulted in higher drag coefficients. The case of square columns at rotated 45° resulted in lowest value of the drag coefficient – this finding may be of practical use when designing a structure in a tsunami-prone area

Finally, only rectangular columns and walls have been investigated. The authors recommend that more complex structure geometries and architectural shapes and orientations should be the subjects of future studies.

References

Al-Faesly, T., Palermo, D., Nistor, I., and Cornett, A. (2012). Experimental modeling of extreme hydrodynamic forces on structural models, *Int. J. Protective Structures*, 3(4), 477–505.

Al-Faesly, T. (2016). Extreme Hydrodynamic Loading on Near-Shore Structures *Doctoral dissertation, University of Ottawa,* Canada.

Árnason H. (2005). Interactions between an incident bore and a free-standing coastal structure. *Doctoral dissertation, University of Washington*, Seattle.

Árnason, H., Petroff, C., and Yeh, H. (2009). Tsunami bore impingement onto a vertical column. *J. Disaster Research*, 4(6), 391–403.

Asakura, R., Iwase, K., Ikeya, T., Kaneto, T., Fujii, N., and Omori, M. (2000) An experiment study on wave force acting on on-shore structures due to overflowing tsunamis. *Proc. Coastal Engineering, JSCE*, 47, 911-915 (in Japanese).

Bruno. L., Fransos. D., Coste. N., Bosco. A. (2010). 3D flow around a rectangular cylinder: A computational study. *J. Wind Eng. Ind. Aerodyn.* 98 (10) 263–276

Bullock, G., Obhrai, C., Peregrine, D., Bredmose, H., 2007. Violent breaking wave impacts. Part 1: results from large-scale regular wave tests on vertical and sloping walls, *Coast. Eng.* 54 (8), 602-617

Chan, I. and Liu, P.L. (2012). On the runup of long waves on a plane beach, *Journal of Geophysical Research*, 117, 1-17.

Chock G., S.E.1; Robertson I., S.E.2; Kriebel D., P.E.3; Francis M., P.E.4;and Nistor I., P.E.5. (2013). Tohoku, Japan, Earthquake and Tsunami of 2011: Performance of Structures under Tsunami Loads. *ASCE*.

Chanson, H. (2006). Tsunami surges on dry coastal plains: application of dam break wave equations. *Coast. Eng. J*. 48 (04), 355–370.

Chanson, H., (2009). Application of the method of characteristics to the dam break wave problem, J. *Hydraul. Res*. 47 (1), 41–49.

Cross, R.H. (1967). Tsunami Surge Forces, *J. Waterways Harbor Div*. 93, 201–231.

Douglas, S., Nistor, I. (2015). On the effect of bed condition on the development of tsunami-induced loading on structures using OpenFOAM®. *Natural Hazards*, 76(2), 1335-1356.

FEMA P646. (2012). Guidelines for design of structures for vertical evacuation from tsunamis, *Federal Emergency Management Agency*, Washington, D.C.

Fujima, K, Achmad, F., Shigihara, Y., and Mizutani, N. (2009) Estimation of Tsunami Force Acting on Rectangular Structures, *Journal of Disaster Research*, Vol. 4, No. 6, pp. 404–409.

Ghobarah, A., Saatcioglu, M., Nistor, I. (2006). The impact of 26 December 2004 earthquake and tsunami on structures and infrastructure, *Engineering Structures*, Elsevier, 28(2), 312-326.

Gupta, V. P. and Goyal, S. C. (1975). Hydrodynamic forces on bridge piers, *Journal of the Institution of Engineers (India)*, Civil Engineering Division 56:12–16.

Hirt, C. W. and Nichols, B. D. (1981). Volume of fluid (VOF) method for the dynamics of free boundaries. *Journal of Computational Physics*, 39:201–225.

Kihara, N.,et al., 2015. Large-scale experiments on tsunami-induced pressure on a vertical tide wall, *Coast. Eng*. 99, 46-63.

Lauber, G. and Hager, W. H. (1998). Experiments to dam-break wave: horizontal channel. *Journal of Hydraulic Research*, 36(3), 291-307.

Launder, B.E. and Spalding, D.B. (1974). The numerical computation of turbulent flows. *Computer Methods in Applied Mechanics and Engineering*, 3(2), 269–289.

Linton, D., Gupta, R., Cox, D., Lindt, J., Oshnack, M. and Clauson, M. (2013). Evaluation of tsunami loads on wood-frame walls at full scale, *J. Structural Engineering*, 139 (8), 1318-1325.

Liu, P. L.-F., Y.-S. Cho, M. J. Briggs, U. Kanoglu, and C. E. Synolakis (1995), Runup of solitary waves on a circular island, *J. Fluid Mech.*, 302, 259 – 285.

Lukkunaprasit, P., Thanasisathit, N., Yeh, H. (2009). Experimental verification of FEMA P646 tsunami loading, *J. Disaster Res.* 4 (6), 410–418.

Madsen P, Fuhrman D, Schaffer H. (2008). On the solitary wave paradigm for tsunamis, *J Geophys Res*. 113(12):1–22.

Mori, N., Takahashi, T. The 2011 Tohoku Earthquake Tsunami Joint Survey Group, 2012.Nationwide post event survey and analysis of the 2011 Tohoku earthquake tsunami. *Coast. Eng. J*. 54 (01), 1–27.

Nistor I, Palermo D, Nouri Y, Murty T, Saatcioglu M (2009). Tsunami forces on structures. In: Kim YC (ed) Handbook of coastal and ocean engineering, *World Scientific, Singapore*. 261–286.

Nouri, Y., Nistor, I., Palermo, D., 2010. Experimental investigation of tsunami impact on free standing structures. C*oastal Engineering Journal, JSCE, World Scientific*, 52(1), 43–70.

Palermo, D., Nistor, I., Al-Faesly, T., Cornett, A., (2013). Impact of tsunami forces on structures. *Int. J. Tsunami Soc.* 32 (2), 58–76

Ramsden, J. D. (1993). Tsunamis: Forces on a vertical wall caused by long waves, bores, and surges on a dry bed, *Ph.D. thesis, California Institute of Technology*, Pasadena, CA.

Ritter, A. (1892). Die fortpflanzung de wasserwellen. *Z. Ver. Dtsch. Ing*. 36 (33), 947–954.

Robertson, I.N., Riggs, H.R., Paczkowski, K. and Mohamed, A. (2011). Tsunami bore forces on walls. *30th International Conference on Ocean, Offshore and Arctic Engineering*, Rotterdam, the Netherlands, June 19-24, 2011.

Rusche, H. (2002). Computational fluid dynamics of dispersed two-phase flows at high phase fractions. *PhD thesis, Imperial College*, London, UK.

Saatcioglu, M., Ghobarah, A., Nistor, I. (2005). Effects of the December 26, 2004 Sumatra earthquake and tsunami on physical infrastructure, Special Issue of the *I. Journal of Earthquake Technology*, 42(4), 79-94.

Shafiei, S., Melville, B. W., Shamseldin, A. Y., (2016). Experimental investigation of tsunami bore impact force and pressure on a square prism. *Coastal Engineering* 110, 1-16.

Shih, T.H., Liou, W.W., Shabbir, A., Yang, Z.,and J. Zhu. (1995). A new k − ϵ eddy viscosity model for high Reynolds number turbulent flows - Model development and validation. *Computers Fluids*, 24(3), 227-238.

Sohankar. A. (2008). Large eddy simulation of flow past rectangular-section cylinders: Side ratio effects. *J. Wind Eng. Ind. Aerodyn*. 96 (08) 640–655.

St-Germain, P. (2012). Numerical modeling of tsunami-induced hydrodynamic forces on free-standing structures using the SPH method. *M.A.Sc. thesis, University of Ottawa*, Ottawa, Canada.

St-Germain, P., Nistor, I., Townsend, R., and Shibayama, T. (2014). Smoothed particle hydrodynamics numerical modeling of structures impacted by tsunami bores. *J. Waterway, Port, Coastal, Ocean Eng*., 140 (1), 66-81.

Synolakis, C. E., (1987). The runup of solitary waves, *J. Fluid Mech*., 185, 523 – 545.

Tian. X.,Ong. M.K., Yang. J., Myrhaug. D.,(2013) Unsteady RANS simulations of flow around rectangular cylinders with different aspect ratios. *Ocean Engineering* 58 (13) 208–216.

Weller, H., (2002). Derivation modelling and solution of the conditionally averaged two-phase flow equations. *Technical Report TR/HGW/02*, Nabla Ltd.

Wilcox, D.C. (1988). Re-assessment of the scale-determining equation for advanced turbulence models. *AIAA Journal*, 26(11), 1299-1310.

Yakhot, V., Orszag, S.A., Thangam, S., Gatski,T.B. and Speziale, C.G. (1991). Development of turbulence models for shear flows by a double expansion technique. *Physics of Fluids A*, 4(7), 1510-1520.

Yeh, H. (2006). Maximum Fluid Forces in the Tsunami Runup Zone. *Journal of Waterway*, Port, Coastal, and Ocean Engineering, 132(6), 496-500.

Yeh, H. (2007). Design tsunami forces for onshore structures. *Journal of Disaster Research*, 2(6), 531-536.

Yeh, H., Francis, M., Peterson, C., Katada, T., Latha, G., Chadha, R.K., Singh, J.P., Rahghuraman, G., (2007). Effects of the 2004 Great Sumatra Tsunami: Southeast Indian Coast. *Journal of Waterway, Port, Coastal, and Ocean Engineering*, 133, pp. 382-400.

Yeh, H., Sato, S. and Tajima, Y. (2013). The 11 March 2011 East Japan Earthquake and Tsunami: Tsunami effects on coastal infrastructure and buildings. *Pure and Applied Geophysics*, 170, 1019-1031.